

Terahertz-driven coherent magnetization dynamics in labyrinth-type domain networks

M. Riepp ^{1,2,*}, A. Philippi-Kobs,^{2,3} L. Müller ², W. Roseker ², R. Rysov ², R. Frömter ⁴, K. Bagschik,² M. Hennes ⁵,
 D. Gupta ¹, S. Marotzke ^{2,3}, M. Walther ², S. Bajt ^{6,7}, R. Pan ², T. Golz ², N. Stojanovic ⁸,
 C. Boeglin ¹ and G. Grübel^{2,†}

¹*Institut de Physique et Chimie des Matériaux de Strasbourg, UMR 7504, Université de Strasbourg, CNRS, 67000 Strasbourg, France*

²*Deutsches Elektronen-Synchrotron DESY, Notkestraße 85, 22607 Hamburg, Germany*

³*Institut für Experimentelle und Angewandte Physik, Christian-Albrechts-Universität zu Kiel, Leibnitzstraße 19, 24098 Kiel, Germany*

⁴*Institute of Physics, Johannes Gutenberg-Universität Mainz, Staudinger Weg 7, 55128 Mainz, Germany*

⁵*Sorbonne Université, CNRS, Institut des NanoSciences de Paris, INSP, UMR7588, F-75005 Paris, France*

⁶*Center for Free-Electron Laser Science CFEL, Deutsches Elektronen-Synchrotron DESY, Notkestr. 85, 22607 Hamburg, Germany*

⁷*The Hamburg Centre for Ultrafast Imaging, Universität Hamburg, Luruper Chaussee 149, 22761 Hamburg, Germany*

⁸*Institute for Optical Sensor Systems, Deutsches Zentrum für Luft- und Raumfahrt, Rutherfordstraße 2, 12489 Berlin, Germany*



(Received 25 June 2024; accepted 12 August 2024; published 3 September 2024)

The controlled manipulation of spins on ultrashort timescales is among the most promising solutions for novel high-speed and low-power-consumption spintronic and magnetic recording applications. To do so, terahertz (THz) light pulses can be used to drive coherent magnetization dynamics in ferromagnetic thin films. We were able to resolve these dynamics on the nanoscale employing THz-pump x-ray resonant magnetic scattering from the labyrinth-type domain network of a Co/Pt multilayer with perpendicular magnetic anisotropy. Our results reveal THz-driven ultrafast demagnetization as well as coherent local magnetization oscillations at the THz fundamental frequency of 2.5 THz. We observe a temporal lag between femtosecond demagnetization and the start of the coherent magnetization oscillations that can be understood by a time-dependent damping. The dynamics of the domain and domain-wall contributions are found to be highly correlated, suggesting the applicability of THz spin control in magnetic nanostructures.

DOI: [10.1103/PhysRevB.110.094405](https://doi.org/10.1103/PhysRevB.110.094405)

I. INTRODUCTION

Understanding spin dynamics driven by ultrashort light pulses is of key importance for developing faster and more energy efficient spintronic and magnetic recording technologies. A promising path to the controlled manipulation of spins on ultrafast timescales is the use of light pulses with frequencies in the terahertz (THz) regime ($\nu_{\text{THz}} \approx 0.1\text{--}10 \times 10^{12}$ Hz) [1–3]. Theory predicts that, in contrast to incoherent ultrafast demagnetization induced by femtosecond optical laser pulses with frequencies in the infrared (IR) regime ($\nu_{\text{IR}} \approx 10^{14}$ Hz) [4], the THz electric field \mathbf{E}_{THz} can induce coherent ultrafast demagnetization at low energy transfer to the sample [5]. Moreover, the THz magnetic field \mathbf{H}_{THz} is capable of driving coherent magnetization dynamics [6–8] and, at high intensities, even an ultrafast reversal of the magnetization direction [9–12]. Due to a photon energy on the order of 1 meV, the THz-induced heating is small compared to IR laser excitation, promising better control over the ultrafast spin dynamics in THz spintronics and THz magnetic recording. Today's materials used for magnetic recording are polycrystalline ferromagnetic thin films with perpendicular magnetic anisotropy

(PMA) and few-nanometer-sized magnetic grains. Experiments on THz-driven spin dynamics, however, have mainly addressed homogeneously magnetized thin films with negligible magnetic anisotropy [7,13–18], whereas the physics in magnetic nanostructures with PMA is largely unknown.

In this article, we report on THz-driven magnetization dynamics in nonhomogeneously magnetized thin films, i.e., the labyrinth-type domain network $m_z(\mathbf{r})$ of a Co/Pt multilayer with PMA. We conducted THz-pump x-ray resonant magnetic scattering (XRMS) to resolve these dynamics with femtosecond time and nanometer spatial resolution [19–23]. The response of $m_z(\mathbf{r})$ shows significant differences depending on the THz pump fluence used. For low-fluence excitation with a filtered THz spectrum ($\nu < 6.0$ THz), m_z undergoes an ultrafast quenching and recovery within 1 ps. For high-fluence excitation with an unfiltered THz spectrum, a steplike quenching within 2 ps is observed, followed by oscillations in resonance with the THz fundamental frequency $\nu_0 = 2.5$ THz. The data are consistent with incoherent and coherent ultrafast magnetization dynamics driven by the \mathbf{E}_{THz} - and \mathbf{H}_{THz} -field components. To understand both the low- and high-fluence behaviors, we introduce a time-dependent damping that is determined by the interplay of lattice heating and PMA reduction. The coherent m_z dynamics are found to be associated with correlated dynamics of the domain state's form factor, which is interpreted as successive broadening and narrowing of the domain walls.

*Contact author: matthias.riepp@ipcms.unistra.fr

†Present address: European X-Ray Free-Electron Laser Facility GmbH, Holzkoppel 4, 22869 Schenefeld, Germany.

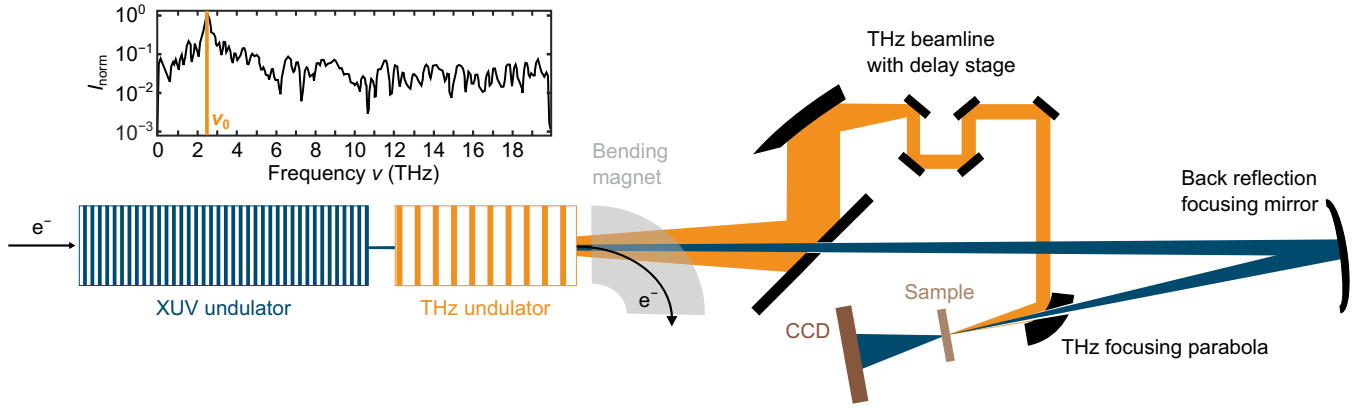


FIG. 1. Schematics of the THz-pump–XRMS probe experiment at the BL3 instrument of FLASH. Relativistic electron bunches consecutively traverse the XUV and THz undulator, producing intrinsically synchronized THz-pump and FEL-probe pulses. The two pulses are delayed in time via a delay stage and focused quasicollinearly onto the sample via a parabolic mirror and a back-reflection multilayer mirror, respectively. The ultrafast magnetization dynamics were measured by time-resolved XRMS in transmission using a CCD that records the scattered XUV light $I(\mathbf{q})$ from the labyrinth-type domain network $m_z(\mathbf{r})$ at pump-probe delay times $-2 < t < 4$ ps. The insert shows the (unfiltered) THz-pump spectrum with the fundamental frequency $\nu_0 = 2.5$ THz.

II. RESULTS AND DISCUSSION

A. Experimental details

To investigate coherent magnetization dynamics on nanometer length scales, we employed a THz-pump–XRMS-probe experiment at the BL3 instrument of the free-electron laser (FEL) FLASH (Fig. 1). The BL3 instrument comprises a planar electromagnetic THz undulator with nine full periods that was tuned to generate linearly polarized pump pulses with a fundamental frequency $\nu_0 = 2.5$ THz (pulse duration of 3.6 ps). The spectrum of the multicycle THz pulses generated at BL3 is broadband, containing frequency components up to the IR regime (see the THz spectrum in Fig. 1). We call this the unfiltered THz radiation. A pump-pulse intensity of $23 \mu\text{J}$ measured by a radiometer [24] and a beam size of $200 \times 160 \mu\text{m}^2$ measured by a fluorescent screen at the sample position yield pump fluence $F_{\text{THz}} = 92 \text{ mJ cm}^{-2}$. This corresponds to electric- and magnetic-field amplitudes $E_{\text{THz}} = 4 \text{ MV cm}^{-1}$ and $\mu_0 H_{\text{THz}} = 1.4 \text{ T}$, respectively. Alternatively, a long-pass filter blocking frequency components $\nu \gtrsim 6.0$ THz was inserted in the THz beamline. For this filtered THz radiation, the pump fluence is reduced by at least a factor of 4 [25]. It is worth mentioning that the existence of coherent magnetization dynamics at THz frequencies was explained by the inertia of the magnetization causing a *nutaton*, i.e., a trembling of the magnetization vector around the effective magnetic field [26–29]. For linearly polarized THz pulses incident normal on a thin film with PMA ($\mathbf{k} \parallel \mathbf{m}$), the Zeeman torque driving such nutation dynamics $\mathbf{T} = \mathbf{m} \times \mathbf{H}_{\text{THz}}$ is maximized (for both vertical and horizontal polarization orientations).

The THz pulses were used to excite the labyrinth-type domain network $m_z(\mathbf{r})$ of a Co/Pt multilayer with PMA. An example of $m_z(\mathbf{r})$ is shown in Fig. 2(a). Here, $m_z = M_z/M_s$ is the local magnetization z component normalized to its value at saturation (room temperature). The response of $m_z(\mathbf{r})$ to THz pumping was measured by means of XRMS using ultrashort FEL pulses from FLASH at variable pump-probe delay time t . Details on the FEL-probe-pulse properties and the measurement procedure are given in Appendix A. The

normalized scattering image $I(\mathbf{q}, t = -1 \text{ ps})$ obtained from the labyrinth-type domain network used in this experiment is shown in Fig. 2(b). In the kinematic limit using linearly polarized x rays, the scattered intensity is given by pure charge- and pure magnetic-scattering contributions, $I(\mathbf{q}) = I_c(\mathbf{q}) + I_m(\mathbf{q})$ [30]. For polycrystalline thin films and the region of q space investigated here, $I_c(\mathbf{q})$ is orders of magnitude smaller than $I_m(\mathbf{q})$ [31]. Hence, $I_c(\mathbf{q}) \approx 0$. $I_m(\mathbf{q})$ were corrected by dark images and normalized to the average FEL-pulse intensity measured by a beam stop photodiode [32]. We mask parasitic scattering like the high-intensity streaks in the center of the image and take the azimuthal average of $I_m(\mathbf{q})$ to reduce the two-dimensional (2D) to a one-dimensional (1D) intensity distribution [see Fig. 2(c)]. By that, we treat the 2D domain network as a 1D chain of up- and down-magnetized domains with average domain characteristics. For analysis of the resulting magnetic-scattering intensity $I_m(q)$, we employ a Lorentzian empirical fitting function [31],

$$I_m(q) = \underbrace{e^{-2q/q_w}}_{F(q)^2} \left[\underbrace{m_0 + \frac{m_1}{\left(\frac{q-q_1}{w_1}\right)^2 + 1}}_{S(q)^2} \right]^2. \quad (1)$$

The first term outside of the square brackets is the form factor $F(q)^2$, which is associated with the magnetic unit cell in real space. It is determined by the domain-wall (DW) parameter q_w and accounts for the asymmetric shape of $I_m(q)$. The term in the square brackets is the magnetic structure factor $S(q)^2$ corresponding to the spatial arrangement of magnetic domains, i.e., the basic magnetic lattice, in real space. It consists of a linear superposition of random uniform spatial fluctuations m_0 and the first-order Lorentzian diffraction peak with amplitude m_1 , position q_1 , and linewidth w_1 . Let us emphasize that Eq. (1) is purely phenomenological. The same functionality, however, has been shown to fit scattering data from time-resolved XRMS up to the fifth diffraction order with excellent accuracy by substituting $S(q)^2$ with a sum of Lorentzian functions [31]. A fit of Eq. (1) to $I_m(q, t = -1 \text{ ps})$

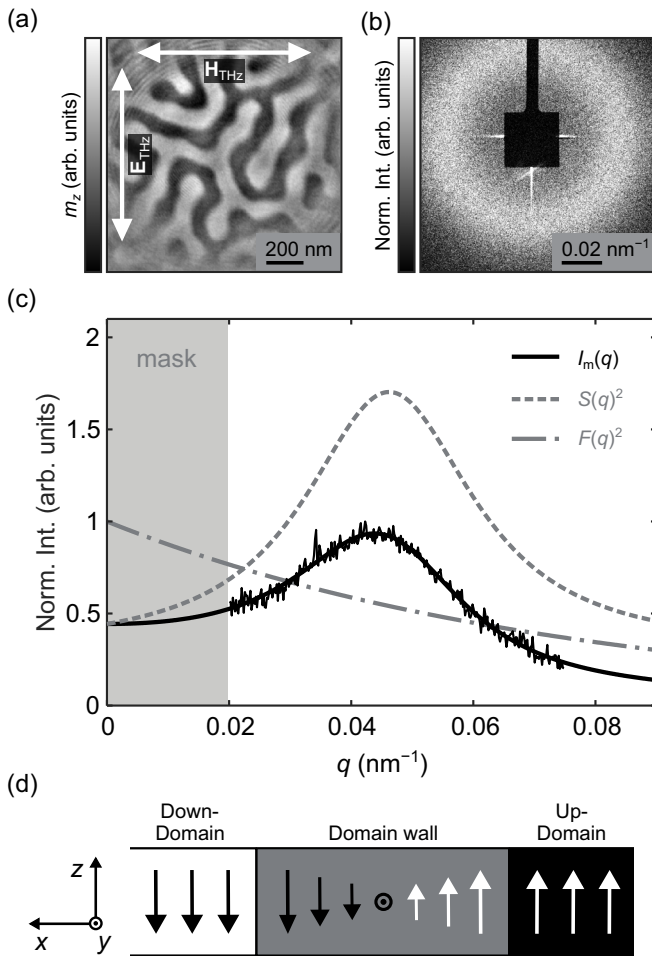


FIG. 2. Form- and structure-factor contributions in time-resolved XRMS. (a) Fourier-transform holography image of the typical labyrinth-type domain network $m_z(\mathbf{r})$ in Co/Pt multilayers showing up- and down-magnetized domains as dark and bright contrast. Arrows indicate the propagation directions of the electric- and magnetic-field components $\mathbf{E}_{\text{THz}}(t) = (0, E_y(t), 0)$ and $\mathbf{H}_{\text{THz}}(t) = (H_x(t), 0, 0)$. (b) The normalized magnetic scattering image $I_m(\mathbf{q}, t = -1 \text{ ps})$ obtained from $m_z(\mathbf{r})$ of the Co/Pt multilayer used in this experiment. (c) Corresponding azimuthal average of the magnetic scattering intensity $I_m(q, t = -1 \text{ ps})$. Included are a fit to the data using Eq. (1) and its individual contributions, i.e., the form factor $F(q)^2$ and the structure factor $S(q)^2$. $I_m(q)$ and $S(q)^2$ are normalized to the maximum of $I_m(q)$ for clarity. (d) One-dimensional illustration of the individual contributions to $I_m(q)$ in real space: domain walls correspond to the magnetic unit cell; up- and down-magnetized domains correspond to the magnetic lattice.

is shown in Fig. 2(c) together with the individual contributions $F(q)^2$ and $S(q)^2$. An illustration of the individual contributions in real space is given in Fig. 2(d). The exponential form factor contribution $q_w = 0.1446 \pm 0.0118 \text{ nm}^{-1}$ can be interpreted as the DW width $\delta_m = 2\pi q_w^{-1} = 43.4 \pm 3.5 \text{ nm}$. Labyrinth-type domain networks of Co/Pt multilayers with PMA exhibit Bloch-type DW character with a width defined by $\delta_B = \pi \sqrt{A_{\text{ex}}(|K_1 + K_2|)^{-1}}$ [33]. Using the measured $K_1 = 19.6 \text{ kJ m}^{-3}$ and $K_2 = -159.1 \text{ kJ m}^{-3}$ (see Appendix B), as well as exchange stiffness $A_{\text{ex}} = 23.3 \text{ pJ m}^{-1}$ in Co/Pt

multilayers with PMA and an individual Co-layer thickness of 0.8 nm [34], we obtain $\delta_B = 40.6 \text{ nm}$, in good agreement with δ_m determined by XRMS. Furthermore, the magnetic structure of the domain network is characterized by $q_1(t = -1 \text{ ps}) = 0.0466 \pm 0.0004 \text{ nm}^{-1}$, corresponding to an average domain period $\xi_m = 2\pi/q_1 = 135.3 \pm 1.2 \text{ nm}$, and $w_1(t = -1 \text{ ps}) = 0.0199 \pm 0.0011 \text{ nm}^{-1}$, corresponding to an average lateral correlation length $\lambda_m = 2\pi/w_1 = 316.1 \pm 17.5 \text{ nm}$.

B. Ultrafast magnetization dynamics driven by low- and high-fluence THz pulses

In the following, we discuss the response of the magnetization z component, given by the amplitude m_1 of the magnetic structure factor $S(q)^2$, upon excitation with the filtered and unfiltered THz pulses. Relative changes $\Delta m_1 - 1$ are presented in Figs. 3(a) and 3(b), together with the H_{THz} -field traces measured by electro-optical sampling (EOS) before the respective measurements.

The response of m_1 to the filtered THz pulses is an ultrafast demagnetization of about 16% within $\tau_d \approx 400 \text{ fs}$ followed by an equally fast and full recovery [Fig. 3(a)]. The maximum degree of 16% agrees well with the observations in a 15 nm Co thin film and can be explained by E_{THz} -field-driven ultrafast demagnetization [7]. According to time-dependent density functional theory (TD-DFT), strong E_{THz} fields are capable of driving a coherent displacement of electrons accompanied by a very efficient spin-orbit-coupling-mediated demagnetization [5]. For the case of monochromatic THz radiation with $\nu_0 = 2.5 \text{ THz}$, one could therefore expect a steplike reduction of m_1 for each half cycle of the E_{THz} field, i.e., $\tau_d = 0.5/\nu_0 = 200 \text{ fs}$ per demagnetization step. We speculate that the slower dynamics observed in this experiment are due to the polychromaticity of the THz radiation ($0 < \nu \lesssim 6.0 \text{ THz}$) causing a more incoherent demagnetization driven by the different E_{THz} -field components. In combination with the low fluence of the filtered THz pulses, this could explain why no further demagnetization steps within the 3.6 ps pulse duration but an ultrafast recovery is observed. Calculating the absorption for the highest-frequency component $\nu = 6.0 \text{ THz}$ via the transfer matrix method, we obtain an absorbed fluence of only about 0.7 mJ cm^{-2} . For low-fluence excitation, incoherent ultrafast demagnetization is known to be followed by an ultrafast magnetization recovery due to efficient energy equilibration among electron, spin, and phonon subsystems. We will show in the next section that $\Delta m_1(t) - 1$ can be explained by the convolution of incoherent ultrafast demagnetization at low fluences and strongly damped coherent oscillations in the presence of PMA.

The situation completely changes when exciting the Co/Pt multilayer with the unfiltered THz pulses [Fig. 3(b)]. Now, m_1 undergoes a steplike demagnetization, reaching a maximum degree of 75% after 2 ps . The increase in the maximum degree of demagnetization can be understood by the additional frequency components $\nu > 6.0 \text{ THz}$ and the associated increase in the pump fluence. Employing the transfer matrix method as before, we obtain a 10 times higher absorbed fluence for $\nu = 20.0 \text{ THz}$, which is the highest frequency component with $I_{\text{norm}}(\nu) > 0.01 I_{\text{norm}}(\nu_0)$. The steplike demagnetization qualitatively agrees with the E_{THz} -field-driven coherent

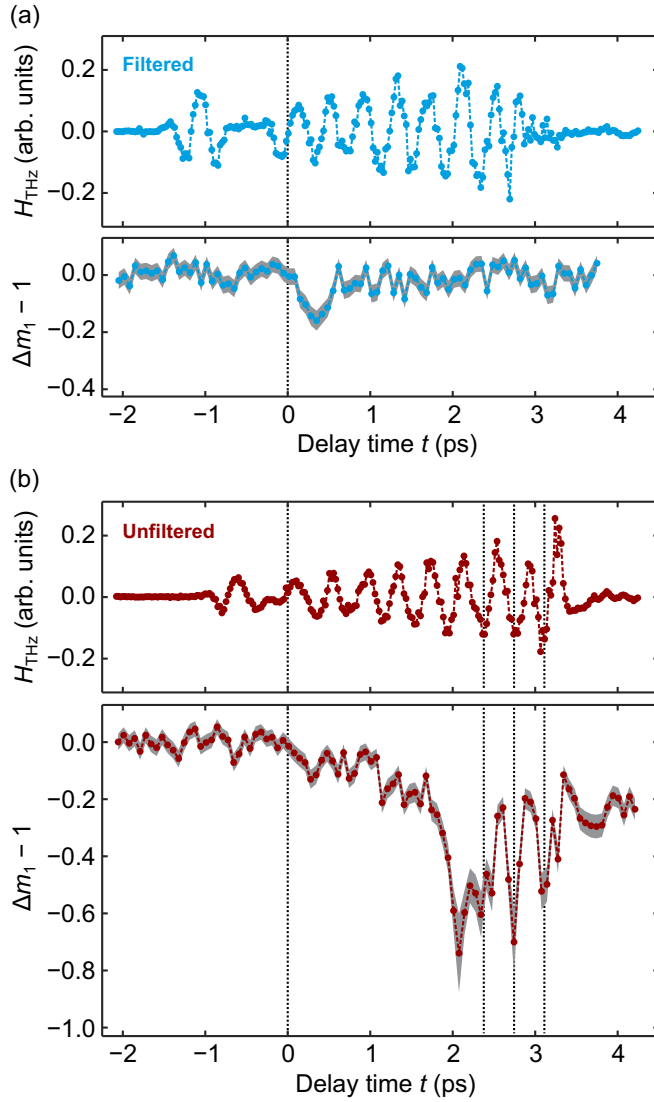


FIG. 3. Ultrafast magnetization dynamics driven by low- and high-fluence THz pulses. (a) H_{THz} -field trace of the filtered THz pulses determined by EOS (top) and the corresponding response of the magnetization z component $\Delta m_1(t) - 1$ (bottom). The incident fluence of the filtered THz pulses is $F_{\text{THz}} < 23 \text{ mJ cm}^{-2}$. (b) The same as (a), but for the unfiltered THz pulses (incident fluence $F_{\text{THz}} \approx 92 \text{ mJ cm}^{-2}$). The so-called edge radiation $H_{\text{THz}}(t \approx -1 \text{ ps})$ in (a) and (b) originates from the electron bunches crossing the edge of the THz undulator. Gray-shaded areas are fit errors. Vertical dotted lines are guides to the eye.

demagnetization predicted by TD-DFT [5]. Demagnetization steps with a duration of about $0.8 \text{ ps} = 2/\nu_0$, however, are much longer than predicted, presumably due to the presence of incoherent demagnetization, as mentioned above. At high fluences, incoherent ultrafast demagnetization is known to be followed by significantly slower recovery dynamics on the picosecond timescale. In addition to these slower recovery dynamics, we observe oscillations of the magnetization z component with an amplitude of about $\pm 20\%$ in resonance with the THz fundamental frequency $\nu_0 = 2.5 \text{ THz}$. This is consistent with coherent magnetization oscillations in the sense of nutation dynamics, a consequence of the H_{THz} field

exerting a Zeeman torque on the magnetization [7,17]. The temporal lag of about 2 ps, however, is rather surprising, as typically, an instantaneous coherent response ($t = 0$) is observed in THz-pump-probe experiments. In comparison with previous studies, we have to consider that the Co/Pt multilayer used in this experiment exhibits PMA, i.e., an energetic minimum for aligning the magnetization along the z axis. We will show in the following section that $\Delta m_1(t) - 1$ can be explained by a convolution of incoherent ultrafast demagnetization at high fluences and coherent m_z oscillations with a temporal lag that is determined by the heat-induced reduction of PMA.

C. Model for fluence-dependent ultrafast magnetization dynamics

In order to understand the response of m_1 to both the filtered and unfiltered THz excitation, we model $\Delta m_1(t) - 1$ via the convolution of incoherent ultrafast demagnetization $\Delta m_i(t) - 1$ and coherent magnetization oscillations $\Delta m_c(t)$ following, e.g., [14,17,25]:

$$\Delta m_1(t) - 1 = [(\Delta m_i(t) - 1)\Theta(t)] * \Delta m_c(t). \quad (2)$$

Here, $\Theta(t)$ is the Heaviside function accounting for the demagnetization onset at $t = 0$. We treat the incoherent contribution $\Delta m_i(t)$ as pure thermal demagnetization induced by an IR pulse with $\lambda_i = 800 \text{ nm}$. Obviously, this is an oversimplification as both the filtered and unfiltered THz pulses contain a broad frequency spectrum. In our approach we cast all E_{THz} -field-induced contributions, whether they are coherent or incoherent electronic excitations, in one $\Delta m_i(t) - 1$ that is comparable to what is known from IR-induced ultrafast demagnetization. The incoherent contribution is simulated within the UDKM1DSIM toolbox [35] that contains the microscopic three-temperature model (M3TM) with heat diffusion along the sample z direction (see Appendix C). We simulated $\Delta m_i(t)$ for a number of fluences and selected the ones that match the experimentally observed maximum degrees of demagnetization. This is the case for fluence $F_i = 4 \text{ mJ cm}^{-2}$ (filtered) and $F_i = 18 \text{ mJ cm}^{-2}$ (unfiltered). Results from simulating $\Delta m_i(t)$ for different fluences via the M3TM are presented in Fig. 4(a). The corresponding electron- and phonon-temperature transients are given in Appendix C.

The coherent contribution $\Delta m_c(t)$ is empirically modeled via the product of the H_{THz} -field trace and a time-dependent damping

$$D(t) = e^{-\left(1 - \frac{k_B T_p(t)}{k_B T_C}\right)t}, \quad (3)$$

where $V = 10 \times 10 \times 10 \text{ nm}^3$ is the volume of a single magnetic grain (macrospin approximation). Even though it is empirically derived, we note that our model for $D(t)$ is inspired by the thermal stability of the magnetization direction in nanoscale magnetic particles obeying Boltzmann statistics. The phonon-temperature transients $T_p(t)$ are known from the M3TM simulations, and the anisotropy transients are calculated according to [36]

$$K_1(T_p(t)) = K_{1,0} m(T_p(t))^{10}. \quad (4)$$

We use $m(\tau) = [1 - s\tau^{3/2} - (1 - s)\tau^{5/2}]^{1/3}$, with the reduced temperature $\tau(t) = T_p(t)/T_C$, and $s = 0.11$ for fcc Co [37].

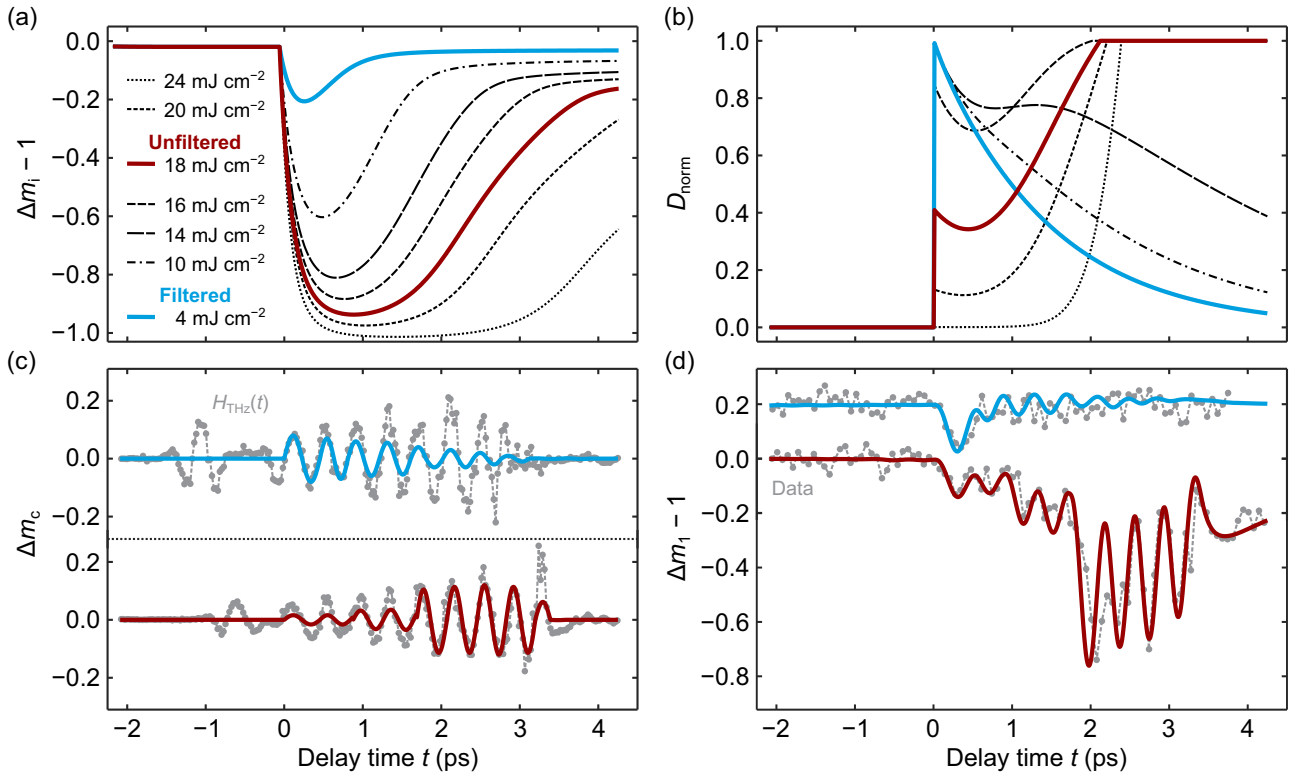


FIG. 4. Model for fluence-dependent ultrafast magnetization dynamics. (a) Incoherent contribution $\Delta m_i(t) - 1$ determined from M3TM simulations using $F_i = 4\text{--}24 \text{ mJ cm}^{-2}$. Magnetization transients that were found to match the experimental data are shown in blue (filtered) and red (unfiltered). (b) Time-dependent damping $D_{\text{norm}}(t)$ as given by Eq. (3). Details are given in the text. (c) Coherent magnetization oscillations $\Delta m_c(t) = H_{\text{THz}}(t)D_{\text{norm}}(t)$. (d) Final model for the transient magnetization z component $\Delta m_1(t) - 1$ given by a convolution of the incoherent [in (a)] and coherent [in (c)] contributions.

Furthermore, we use $K_{1,0} = 20 \text{ kJ m}^{-3}$ at room temperature and a Curie temperature $T_C = 840 \text{ K}$ (see measurements in Appendix B). The calculated $K_1(T_p(t))$ are given in Appendix C.

In the limit of low fluences, $k_B T_p(t) \ll K_1(t)V$ at all times; i.e., the pump-induced heating of the lattice is too weak to induce a substantial reduction of PMA. In this case, $D(t) = D_{\text{norm}}(t)$ becomes an exponential decay [Fig. 4(b)], and the coherent oscillations $\Delta m_c(t)$ are strongly damped [Fig. 4(c)]. In the limit of high fluences, $D(t)$ diverges, which corresponds to the unphysical case of strongly amplified oscillations. We therefore restrict our model to values of $D_{\text{norm}} \leq 1$. In the case of $D(t) > 1$, we normalize Eq. (3) to its value of minimum magnetic anisotropy [$t < t(K_{1,\text{min}})$] and set $D_{\text{norm}}(t) = 1$ for $t > t(K_{1,\text{min}})$. In other words, D_{norm} dynamically changes as K_1 decreases and reaches the regime of the undamped coherent oscillations ($D_{\text{norm}} = 1$) when $K_1 = K_{1,\text{min}}$ [Fig. 4(b)]. In the case of high fluences, $D_{\text{norm}}(t)$ is small for $t \approx 0$, and the coherent oscillations $\Delta m_c(t)$ develop in amplitude until $t \approx 2 \text{ ps}$ [Fig. 4(c)].

The convolution of $\Delta m_i(t)$ and $\Delta m_c(t)$ is presented for the filtered and unfiltered THz excitations in Fig. 4(d). The model accurately reproduces the different features of both magnetization transients for the entire measured time range. For the unfiltered THz pulses, deviations that exceed the experimental noise at $t \approx 2 \text{ ps}$ could originate from the strong electromagnetic field and the associated nonlinearities in the

magnetization response [15]. Note that for the case of a sample with negligible K_1 , the criterion $D(t) > 1$ holds from the start ($t = 0$), and our model predicts the instantaneous (undamped) coherent response to the H_{THz} field observed, e.g., in [7,17]. Furthermore, our model is in qualitative agreement with the increasing temporal lag of the coherent response with increasing magnetic anisotropy from fcc to bcc to hcp Co [38] as well as with a time-dependent damping factor predicted by theory [39]. It was even suggested in [38] that the coherent magnetization dynamics, including both coherent precession at gigahertz frequencies and nutation at THz frequencies, could be fully described by one time-dependent damping factor that is qualitatively linked to a stronger electron-phonon scattering at subpicosecond timescales and weaker spin-lattice relaxation at longer timescales.

D. THz-driven domain and domain-wall dynamics

Finally, we discuss the effect of THz pumping on the lateral domain configuration. For that we analyze the time evolution of the position q_1 and width w_1 of the magnetic structure factor $S(q)^2$, as well as the time evolution of the DW parameter q_w of the magnetic form factor $F(q)^2$ [Figs. 5(a)–5(c)].

When pumping with the filtered THz pulses, constant fit parameters q_1 , w_1 , and q_w are obtained, which is consistent with the fluence threshold for ultrafast domain and

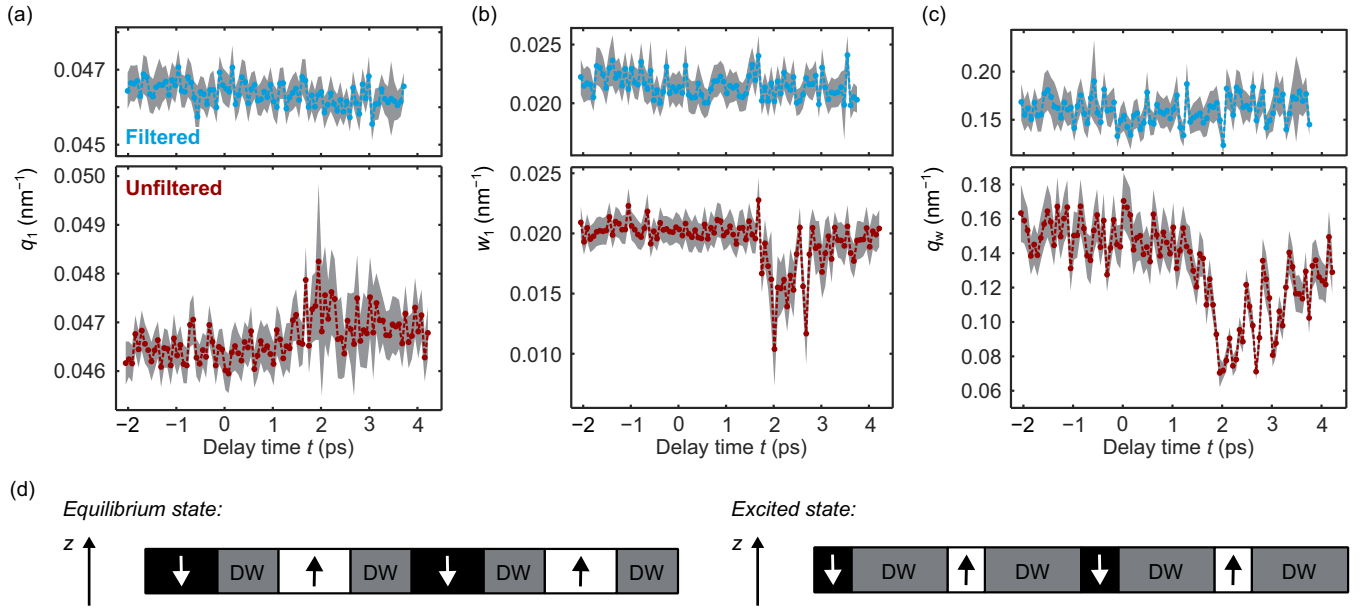


FIG. 5. Ultrafast domain and domain-wall dynamics. (a) and (b) Transient position $q_1(t)$ and width $w_1(t)$ of the domain network's structure factor $S(q, t)^2$. (c) Transient DW parameter $q_w(t)$ of the domain network's form factor $F(q, t)^2$. Results from using the filtered and unfiltered THz pulses are shown in blue and red, respectively. Gray-shaded areas are fit errors. (d) One-dimensional illustration of the equilibrium ($t < 0$) and maximum excited domain network in real space.

DW dynamics in IR-induced ultrafast demagnetization [40]. The parameters q_1 , w_1 , and q_w even remain constant for $t < 2$ ps when pumping with high-fluence THz pulses (unfiltered), demonstrating that the domain network's structure and form maintain their equilibrium size distributions on ultrafast timescales. This is qualitatively different from the ultrafast q_1 shift by 3%–6% to smaller values when using high-fluence IR-pump pulses [40]. Although this shift was originally explained by a broadening of the DWs due to lateral superdiffusive spin transport, more recent experiments suggest ultrafast domain reconfigurations as an explanation, with a larger effect in low-symmetry systems like labyrinth-type domain networks [31,41]. However, no such femtosecond domain reconfigurations can be observed here, even for high-fluence THz excitation. The absence of such ultrafast domain dynamics and, rather, the existence of a lag time that is determined by the time needed to compensate PMA were reported for stripe-domain networks before [42,43]. For compensated PMA and in the presence of small in-plane magnetic fields, the stripes were found to undergo a reorientation along this field direction during magnetization recovery. Upon compensation of PMA ($t \approx 2$ ps), here, the DW parameter q_w undergoes oscillatory dynamics that are highly correlated with the m_1 dynamics in Fig. 3(b). Assuming that q_w is inversely related to the Bloch-wall width, this could be interpreted as a successive broadening and narrowing of DWs between 43 and 89 nm at maximum. A slight increase in q_1 within the error of the fit in combination with a sharp drop in w_1 to almost half its equilibrium value points to an increased long-range order during these coherent oscillations from $\mathcal{O} = q_1/w_1 \approx 2.3$ to $\mathcal{O} \approx 3.0$ at maximum. A situation where the DW width increases while the average domain period remains largely the same is illustrated in

Fig. 5(d). The high degree of correlation between the m_1 and q_w dynamics at $t > 2$ ps directly shows the high degree of correlation between the dynamics of local out-of-plane (z) and in-plane (x, y) magnetization components during the coherent oscillations.

III. CONCLUSIONS

The labyrinth-type $m_z(\mathbf{r})$ of a Co/Pt multilayer with PMA undergoes fluence-dependent ultrafast dynamics upon excitation by multicycle THz pulses. Our results are consistent with E_{THz} -field-driven ultrafast demagnetization and H_{THz} -field-driven coherent local magnetization oscillations. In order to understand both low- and high-fluence results, we introduced a time-dependent damping that is determined by the interplay of lattice heating and PMA reduction. For low pump fluences (filtered), PMA remains largely unaffected and causes a rapid alignment of the magnetization along the equilibrium (z) direction, resulting in strongly damped coherent m_z oscillations. For high pump fluences (unfiltered), PMA undergoes a substantial reduction which enables undamped coherent m_z oscillations upon lattice heating. The time to overcome the anisotropy energy barrier thereby determines the temporal lag of the coherent response, suggesting an upper speed limit for THz-driven magnetization switching in ferromagnets with PMA. The nanometer spatial resolution of time-resolved XRMS revealed correlated dynamics between domain and DW contributions, showing no signs of decorrelation via spin superdiffusion or ultrafast domain rearrangements. Hence, our results suggest the feasibility of controllable spin dynamics in magnetic nanostructures using THz-pump pulses and provide a guideline to tune these dynamics by tailoring PMA and the THz-pump fluence.

ACKNOWLEDGMENTS

We acknowledge DESY (Hamburg, Germany), a member of the Helmholtz Association HGF, for the provision of experimental facilities. Parts of this research were carried out at FLASH. We thank S. Düsterer, M. Temme, and the whole experimental team at FLASH for assistance in using the BL3 instrument. Beam time was allocated for Proposal No. F-20160531. We thank E. Jal, N. Bergéard, and B. Vodungbo for many fruitful discussions, as well as D. Hrabovsky at the MPBT platform of Sorbonne Université for his support with the VSM measurements. We gratefully acknowledge funding by the Deutsche Forschungsgemeinschaft (DFG)–SFB-925–Project ID No. 170620586, the Cluster of Excellence “Advanced Imaging of Matter” of the DFG–EXC-2056–Project ID No. 390715994, the European Union’s Horizon 2020 research and innovation program under Marie Skłodowska-Curie Grant Agreement No. 847471, and the Agence Nationale de la Recherche (ANR) for the project ANR-20-CE42-0012-01 (MEDYNA).

APPENDIX A: TIME-RESOLVED X-RAY RESONANT MAGNETIC SCATTERING

For the THz-pump–XRMS-probe experiment, FLASH was operated in the single-bunch mode providing 60 fs extreme ultraviolet (XUV) probe pulses at a repetition rate of 10 Hz. The XUV undulator was tuned to generate probe pulses with an average self-amplified spontaneous emission spectrum centered around $\lambda_{\text{XUV}} = 20.8$ nm, i.e., a photon energy $E_{\text{XUV}} = 59.6 \pm 0.6$ eV in resonance with the Co $M_{2,3}$ absorption edge [44]. Higher harmonics of the FEL spectrum were blocked by a Si and Zr solid-state filter which, in combination with the back-reflection focusing mirror, attenuates the probe-pulse intensity to about $0.037 \mu\text{J}$. With a beam size

of $52 \times 40 \mu\text{m}^2$, the calculated probe fluence is 2.2 mJ cm^{-2} . As expected for such a moderate fluence, no XUV-induced demagnetization or XUV-induced permanent domain modifications were observed [45,46]. A THz beam with an about 4 times larger diameter than the XUV beam ensured homogeneous excitation of the probed area. Diagnostic tools on the sample holder allowed for measuring coarse temporal as well as spatial overlap of the two beams at the sample position [47]. The scattered intensity was recorded by a CCD with 2048×2048 pixels and a pixel size of $13.5 \mu\text{m}$. A beam stop photodiode was installed centimeters from the detector to block the intense direct FEL beam and, at the same time, monitor FEL-intensity fluctuations for normalization of the data [32]. The scattering statistics were improved by binning 4×4 pixels and accumulating 50 FEL pulse exposures in one exposure of the CCD.

APPENDIX B: SAMPLE PROPERTIES

The sample used in this study was a ferromagnetic Pt(2.0)/[Co(0.8)/Pt(0.8)]₈/Pt(5.0) multilayer grown on a Si₃N₄(50.0) multimembrane substrate via sputtering techniques (numbers are in nanometers). Structural investigations of Co/Pt multilayers fabricated in the same way revealed polycrystallinity with pronounced (1 1 1) texture and a grain size of about 10 nm [48].

The first- and second-order effective magnetic anisotropy constants $K_{1,2}$ were determined by the magneto-optical Kerr effect (MOKE) in polar and longitudinal geometries [Figs. 6(a) and 6(b)]. Polar MOKE measurements revealed magnetic easy-axis behavior along the out-of-plane (OOP) direction with a coercive field $\mu_0 H_c \approx 25$ mT and a saturation field $\mu_0 H_s \approx 150$ mT. Longitudinal MOKE revealed magnetic hard-axis behavior along the in-plane (IP) direction. $K_{1,2}$

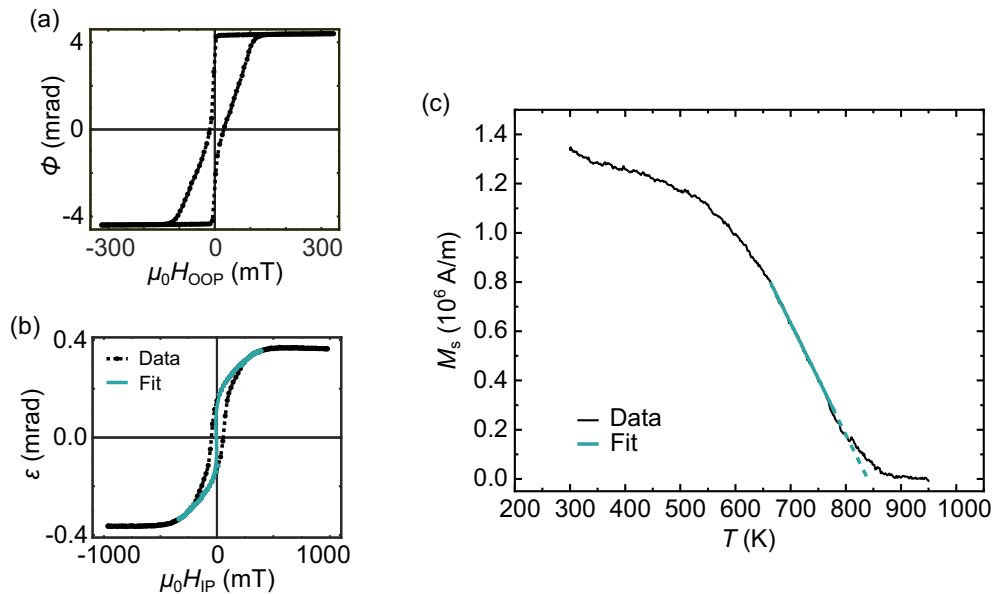


FIG. 6. Static magnetic properties. (a) and (b) Results from polar and longitudinal MOKE at room temperature. The solid line in (b) is a fit to the inverted data $\mu_0 H_{\text{IP}}(\varepsilon)$ for small ε . (c) Temperature dependence of the spontaneous magnetization M_s measured by a vibrating sample magnetometer in external magnetic field $\mu_0 H_{\text{IP}} = 500$ mT. The Curie temperature $T_C \approx 840$ K is estimated via a linear extrapolation at high temperatures.

TABLE I. Material-specific parameters used for the M3TM simulations.

	Co	Pt	Si ₃ N ₄
C_e (J kg ⁻¹ K ⁻¹)	0.0734 T_e [50]	0.0335 T_e [50]	0.0100 T_e^a
C_p (J kg ⁻¹ K ⁻¹)	421 [51]	133 [51]	700 [51]
κ_e (W m ⁻¹ K ⁻¹)	20 ^a	20 ^a	20 ^a
κ_p (W m ⁻¹ K ⁻¹)	100 [51]	71.6 [51]	2.5 [52]
ρ (kg m ⁻³)	8860 [51]	21500 [51]	3190 [51]
$n + ik$	2.53 + 4.88 i [53]	0.60 + 8.38 i [53]	2.00 [51]

^aAssumption.

were determined by fitting the (inverted) hard-axis hysteresis loop with

$$\mu_0 H_{IP}(m_{\parallel}) = \frac{2K_1}{M_s} m_{\parallel} + \frac{4K_2}{M_s} m_{\parallel}^3, \quad (\text{B1})$$

where $M_s = 1.4 \times 10^6$ A m⁻¹ is the spontaneous magnetization in bulk Co at $T = 0$ K and m_{\parallel} is the reduced magnetization component parallel to H_{IP} . A fit of Eq. (B1) to the data yields $K_1 = 19.6 \pm 4.7$ kJ m⁻³ and $K_2 = -159.1 \pm 3.7$ kJ m⁻³. Prior to the FEL beam time, the sample was exposed to alternating OOP magnetic-field cycles with decreasing amplitude and $\mu_0 H_{\max} = 1$ T to generate the labyrinth-type domain network $m_z(\mathbf{r})$ close to the magnetic ground state.

After the experiment, the temperature dependence of the spontaneous magnetization $M_s(T)$ was measured by a vibrating sample magnetometer in external magnetic field $\mu_0 H_{IP} = 500$ mT. The temperature was increased from $T = 300$ K to

$T = 950$ K at a rate of $\Delta T = 10$ K min⁻¹. The Curie temperature $T_C \approx 840$ K was estimated by a linear extrapolation of $M_s(T)$ at high temperatures.

APPENDIX C: M3TM SIMULATIONS

Incoherent ultrafast demagnetization was simulated within the UDKM1DSIM toolbox [35], which contains the microscopic three-temperature model (M3TM) [49], including heat diffusion along the sample z direction,

$$\begin{aligned} C_e \rho \frac{\partial T_e}{\partial t} &= \frac{\partial}{\partial z} \left(\kappa_e \frac{\partial T_e}{\partial z} \right) - G_{ep} (T_e - T_p) + S(z, t), \\ C_p \rho \frac{\partial T_p}{\partial t} &= \frac{\partial}{\partial z} \left(\kappa_p \frac{\partial T_p}{\partial z} \right) + G_{ep} (T_e - T_p), \\ \frac{\partial m_i}{\partial t} &= R m_i \frac{T_p}{T_C} \left[1 - \coth \left(\frac{m_i T_C}{T_e} \right) \right]. \end{aligned} \quad (\text{C1})$$

The first two differentials describe the electron- and phonon-temperature transients, respectively, where C_e and C_p are the heat capacities, κ_e and κ_p are the thermal conductivities, G_{ep} is the electron-phonon coupling parameter, and ρ is the density. The initial heating of the electron system is given by the laser source term $S(z, t)$. Instead of a spin-temperature transient, the M3TM considers a magnetization transient that depends on T_e and T_p , with a shape defined by $R = 8a_{sf} G_{ep} k_B T_C^2 V_{at} \mu_B \mu_{at}^{-1} E_D^{-2}$. Here, $a_{sf} = 0.15$ is the spin-flip probability, k_B is the Boltzmann constant, $T_C = 840$ K is the Curie temperature, $V_{at} = 4\pi r_{at}^3/3$ is the atomic volume with atomic radius $r_{at} = 1.35$ Å, $\mu_{at}/\mu_B = 1.72$ is the atomic magnetic moment in units of the Bohr magneton, and

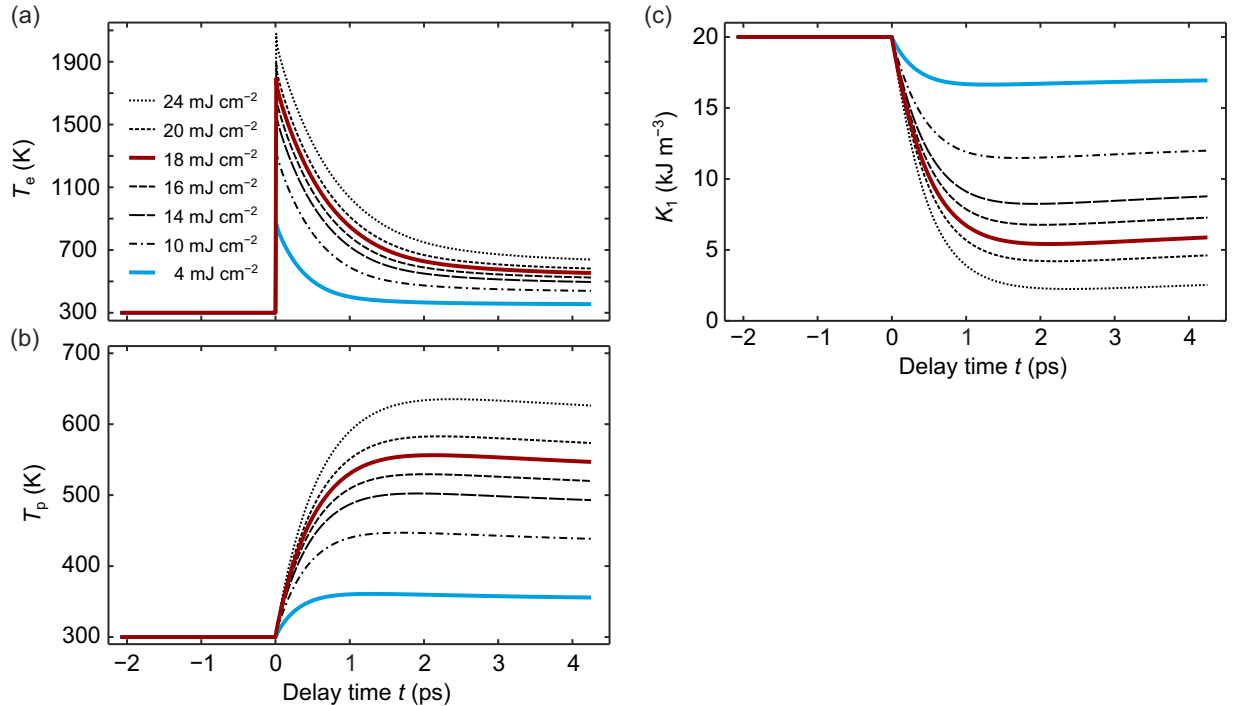


FIG. 7. Results from M3TM simulations. (a) and (b) Transient electron and phonon temperatures $T_e(t)$ and $T_p(t)$ for fluences $F_i = 4$ –24 mJ cm⁻². The transients are obtained from averaging spatiotemporal heat maps, simulated within the UDKM1DSIM toolbox, along the sample z direction. (c) Transient first-order effective magnetic anisotropy $K_1(t)$, calculated as described in the main text.

$E_D = 0.0357 \text{ eV}$ is the Debye energy of Co [49]. For the electron-phonon coupling parameter we take a constant value of $G_{ep} = 1.5 \times 10^{18} \text{ W m}^{-3} \text{ K}^{-1}$ in Co [54]. The UDKM1DSIM toolbox yields a reflectivity of 85.6% and a transmission of 4.5% at $\lambda_i = 800 \text{ nm}$, calculated by the transfer matrix method including multilayer absorption.

Within the UDKM1DSIM toolbox, in the first step, the Pt(2.0)/[Co(0.8)/Pt(0.8)]₈/Pt(6)/Si₃N₄(50) sample structure is generated as a 1D amorphous multilayer with material-specific properties for each subsystem (see Table I). In the second step, the laser source term $S(z, t)$ is defined as a δ -like pulse of high frequency ($\lambda_i = 800 \text{ nm}$) with fluence $F_i = 4$ –

24 mJ cm^{-2} . Note that the influence of the 3.6 ps pump-pulse duration is taken into account via the convolution with the coherent contribution $\Delta m_c(t)$ (see the main text). In the final step, the UDKM1DSIM toolbox calculates spatiotemporal heat maps of the electron temperature, phonon temperature, and magnetization for a certain delay range by solving Eq. (C1) with an ordinary differential equation solver. $T_e(t)$, $T_p(t)$, and $\Delta m_i(t)$ are obtained by taking the heat maps' spatial average along the z direction. $T_e(t)$ and $T_p(t)$ are given in Figs. 7(a) and 7(b), and $\Delta m_i(t)$ is given in the main text. The anisotropy transients $K_1(t)$ shown in Fig. 7(c) were determined from the phonon-temperature transients as described in the main text.

-
- [1] T. Kampfrath, K. Tanaka, and K. A. Nelson, *Nat. Photonics* **7**, 680 (2013).
- [2] J. Walowski and M. Münzenberg, *J. Appl. Phys.* **120**, 140901 (2016).
- [3] A. Barman, G. Gubbiotti, S. Ladak, A. O. Adeyeye, M. Krawczyk, J. Gräfe, C. Adelman, S. Cotozana, A. Naeemi, V. I. Vasyuchka, B. Hillebrands, S. A. Nikitov, H. Yu, D. Grundler, A. V. Sadovnikov, A. A. Grachev, S. E. Sheshukova, J.-Y. Duquesne, M. Marangolo, G. Csaba *et al.*, *J. Phys.: Condens. Matter* **33**, 413001 (2021).
- [4] E. Beaupaire, J.-C. Merle, A. Daunois, and J.-Y. Bigot, *Phys. Rev. Lett.* **76**, 4250 (1996).
- [5] C. Pellegrini, S. Sharma, J. K. Dewhurst, and A. Sanna, *Phys. Rev. B* **105**, 134425 (2022).
- [6] T. Kampfrath, A. Sell, G. Klatt, A. Pashkin, S. Mährlein, T. Dekorsy, M. Wolf, M. Fiebig, A. Leitenstorfer, and R. Huber, *Nat. Photonics* **5**, 31 (2011).
- [7] M. Shalaby, A. Donges, K. Carva, R. Allenspach, P. M. Oppeneer, U. Nowak, and C. P. Hauri, *Phys. Rev. B* **98**, 014405 (2018).
- [8] K. Neeraj, N. Awari, S. Kovalev, D. Polley, N. Z. Hagström, S. S. P. K. Arekapudi, A. Semisalova, K. Lenz, B. Green, J.-C. Deinert, I. Ilyakov, M. Chen, M. Bawatna, V. Scalera, M. d'Aquino, C. Serpico, O. Hellwig, J.-E. Wegrowe, M. Gensch, and S. Bonetti, *Nat. Phys.* **17**, 245 (2021).
- [9] C. H. Back, D. Weller, J. Heidmann, D. Mauri, D. Guarisco, E. L. Garwin, and H. C. Siegmann, *Phys. Rev. Lett.* **81**, 3251 (1998).
- [10] I. Tudosa, C. Stamm, A. B. Kashuba, F. King, H. C. Siegmann, J. Stöhr, G. Ju, B. Lu, and D. Weller, *Nature (London)* **428**, 831 (2004).
- [11] D. Polley, M. Pancaldi, M. Hudl, P. Vavassori, S. Urazhdin, and S. Bonetti, *J. Phys. D* **51**, 084001 (2018).
- [12] K. Neeraj, M. Pancaldi, V. Scalera, S. Perna, M. d'Aquino, C. Serpico, and S. Bonetti, *Phys. Rev. B* **105**, 054415 (2022).
- [13] C. Vicario, C. Ruchert, F. Ardana-Lamas, P. M. Derlet, B. Tudu, J. Luning, and C. P. Hauri, *Nat. Photonics* **7**, 720 (2013).
- [14] S. Bonetti, M. C. Hoffmann, M.-J. Sher, Z. Chen, S.-H. Yang, M. G. Samant, S. S. P. Parkin, and H. A. Dürr, *Phys. Rev. Lett.* **117**, 087205 (2016).
- [15] M. Hudl, M. d'Aquino, M. Pancaldi, S.-H. Yang, M. G. Samant, S. S. P. Parkin, H. A. Dürr, C. Serpico, M. C. Hoffmann, and S. Bonetti, *Phys. Rev. Lett.* **123**, 197204 (2019).
- [16] R. Rouzegar, L. Brandt, L. Nádvorník, D. A. Reiss, A. L. Chekhov, O. Gueckstock, C. In, M. Wolf, T. S. Seifert, P. W. Brouwer, G. Woltersdorf, and T. Kampfrath, *Phys. Rev. B* **106**, 144427 (2022).
- [17] K. Neeraj, A. Sharma, M. Almeida, P. Matthes, F. Samad, G. Salvan, O. Hellwig, and S. Bonetti, *Appl. Phys. Lett.* **120**, 102406 (2022).
- [18] R. Salikhov, I. Ilyakov, L. Körber, A. Kákay, R. A. Gallardo, A. Ponomaryov, J.-C. Deinert, T. V. A. G. de Oliveira, K. Lenz, J. Fassbender, S. Bonetti, O. Hellwig, J. Lindner, and S. Kovalev, *Nat. Phys.* **19**, 529 (2023).
- [19] J. Stöhr and H. C. Siegmann, *Magnetism: From Fundamentals to Nanoscale Dynamics*, Springer Series in Solid-State Sciences Vol. 152 (Springer, Berlin, 2006).
- [20] C. Gutt, L.-M. Stadler, S. Streit-Nierobisch, A. P. Mancuso, A. Schropp, B. Pfau, C. M. Günther, R. Könnecke, J. Gulden, B. Reime, J. Feldhaus, E. Weckert, I. A. Vartanyants, O. Hellwig, F. Staier, R. Barth, M. Grunze, A. Rosenhahn, D. Stickler, H. Stillrich *et al.*, *Phys. Rev. B* **79**, 212406 (2009).
- [21] C. Gutt, S. Streit-Nierobisch, L.-M. Stadler, B. Pfau, C. M. Günther, R. Könnecke, R. Frömter, A. Kobs, D. Stickler, H. P. Oepen, R. R. Fustlin, R. Treusch, J. Feldhaus, E. Weckert, I. A. Vartanyants, M. Grunze, A. Rosenhahn, T. Wilhein, S. Eisebitt, and G. Grübel, *Phys. Rev. B* **81**, 100401(R) (2010).
- [22] B. Vodungbo, J. Gautier, G. Lambert, A. B. Sardinha, M. Lozano, S. Sebban, M. Ducouso, W. Boutu, K. Li, B. Tudu, M. Tortarolo, R. Hawaldar, R. Delaunay, V. López-Flores, J. Arabski, C. Boeglin, H. Merdji, P. Zeitoun, and J. Lüning, *Nat. Commun.* **3**, 999 (2012).
- [23] T. Wang, D. Zhu, B. Wu, C. Graves, S. Schaffert, T. Rander, L. Müller, B. Vodungbo, C. Baumier, D. P. Bernstein, B. Bräuer, V. Cros, S. de Jong, R. Delaunay, A. Fognini, R. Kukreja, S. Lee, V. López-Flores, J. Mohanty, B. Pfau *et al.*, *Phys. Rev. Lett.* **108**, 267403 (2012).
- [24] R. Pan, E. Zapolnova, T. Golz, A. J. Krmpot, M. D. Rabasovic, J. Petrovic, V. Asgekar, B. Faatz, F. Tavella, A. Perucchi, S. Kovalev, B. Green, G. Geloni, T. Tanikawa, M. Yurkov, E. Schneidmiller, M. Gensch, and N. Stojanovic, *J. Synchrotron Radiat.* **26**, 700 (2019).
- [25] X. Liu, E. Jal, R. Delaunay, R. Jarrier, G. S. Chiuzbaian, G. Malinowski, T. Golz, E. Zapolnova, R. Pan, N. Stojanovic, J. Lüning, and B. Vodungbo, *Appl. Sci.* **12**, 1323 (2022).

- [26] M.-C. Ciornei, J. M. Rubí, and J.-E. Wegrowe, *Phys. Rev. B* **83**, 020410(R) (2011).
- [27] S. Bhattacharjee, L. Nordström, and J. Fransson, *Phys. Rev. Lett.* **108**, 057204 (2012).
- [28] E. Olive, Y. Lansac, M. Meyer, M. Hayoun, and J.-E. Wegrowe, *J. Appl. Phys.* **117**, 213904 (2015).
- [29] R. Mondal, M. Berritta, A. K. Nandy, and P. M. Oppeneer, *Phys. Rev. B* **96**, 024425 (2017).
- [30] J. B. Kortright, *J. Electron Spectrosc. Relat. Phenom.* **189**, 178 (2013).
- [31] D. Zusin, E. Iacocca, L. Le Guyader, A. H. Reid, W. F. Schlotter, T.-M. Liu, D. J. Higley, G. Coslovich, S. F. Wandel, P. M. Tengdin, S. K. K. Patel, A. Shabalin, N. Hua, S. B. Hrkac, H. T. Nembach, J. M. Shaw, S. A. Montoya, A. Blonsky, C. Gentry, M. A. Hofer *et al.*, *Phys. Rev. B* **106**, 144422 (2022).
- [32] L. Müller, M. Walther, M. Riepp, A. Philippi-Kobs, W. Jo, W. Roseker, K. Bagschik, R. Frömter, R. Pan, D. Lott, J. Möller, U. Bösenberg, J. Hallmann, A. Rodriguez-Fernandez, M. Scholz, G. Ansaldo, J. Wrigley, A. Zozulya, A. Madsen, and G. Grübel, *J. Phys.: Conf. Ser.* **2380**, 012081 (2022).
- [33] H. Träuble, O. Boser, H. Kronmüller, and A. Seeger, *Phys. Status Solidi B* **10**, 283 (1965).
- [34] P. J. Metaxas, J. P. Jamet, A. Mougin, M. Cormier, J. Ferré, V. Baltz, B. Rodmacq, B. Dieny, and R. L. Stamps, *Phys. Rev. Lett.* **99**, 217208 (2007).
- [35] D. Schick, *Comput. Phys. Commun.* **266**, 108031 (2021).
- [36] J.-Y. Bigot, M. Vomir, L. Andrade, and E. Beaurepaire, *Chem. Phys.* **318**, 137 (2005).
- [37] M. D. Kuz'min, *Phys. Rev. Lett.* **94**, 107204 (2005).
- [38] V. Unikandanunni, R. Medapalli, M. Asa, E. Albisetti, D. Petti, R. Bertacco, E. E. Fullerton, and S. Bonetti, *Phys. Rev. Lett.* **129**, 237201 (2022).
- [39] U. Bajpai and B. K. Nikolić, *Phys. Rev. B* **99**, 134409 (2019).
- [40] B. Pfau, S. Schaffert, L. Müller, C. Gutt, A. Al-Shemmary, F. Büttner, R. Delaunay, S. Düsterer, S. Flewett, R. Frömter, J. Geilhufe, E. Guehrs, C. M. Günther, R. Hawaldar, M. Hille, N. Jaouen, A. Kobs, K. Li, J. Mohanty, H. Redlin *et al.*, *Nat. Commun.* **3**, 1100 (2012).
- [41] N. Z. Hagström, R. Jangid, M. Madhavi, D. Turenne, J. A. Brock, E. S. Lamb, B. Stoychev, J. Schlappa, N. Gerasimova, B. Van Kuiken, R. Gort, L. Mercadier, L. Le Guyader, A. Samartsev, A. Scherz, G. Mercurio, H. A. Dürr, A. H. Reid, M. Arora, H. T. Nembach *et al.*, *Phys. Rev. B* **106**, 224424 (2022).
- [42] N. Berggaard, S. Schaffert, V. López-Flores, N. Jaouen, J. Geilhufe, C. M. Günther, M. Schneider, C. Graves, T. Wang, B. Wu, A. Scherz, C. Baumier, R. Delaunay, F. Fortuna, M. Tortarolo, B. Tudou, O. Krupin, M. P. Miniti, J. Robinson, W. F. Schlotter *et al.*, *Phys. Rev. B* **91**, 054416 (2015).
- [43] V. López-Flores, M.-A. Mawass, J. Herrero-Albillos, A. A. Uenal, S. Valencia, F. Kronast, and C. Boeglin, *J. Phys.: Condens. Matter* **32**, 465801 (2020).
- [44] K. Tiedtke, A. Azima, N. von Barga, L. Bittner, S. Bonfigt, S. Düsterer, B. Faatz, U. Frühling, M. Gensch, Ch. Gerth, N. Guerassimova, U. Hahn, T. Hans, M. Hesse, K. Honkavaar, U. Jastrow, P. Juranic, S. Kapitzki, B. Keitel, T. Kracht *et al.*, *New J. Phys.* **11**, 023029 (2009).
- [45] K. J. Kapcia, V. Tkachenko, F. Capotondi, A. Lichtenstein, S. Molodtsov, L. Müller, A. Philippi-Kobs, P. Piekarczyk, and B. Ziaja, *npj Comput. Mater.* **8**, 212 (2022).
- [46] M. Riepp, L. Müller, A. Philippi-Kobs, M. Walther, W. Roseker, R. Rysov, S. Marotzke, K. Bagschik, J. Buck, R. Frömter, J. Wagner, F. Capotondi, E. Pedersoli, D. Naumenko, M. Kiskinova, H. P. Oepen, J. Viehhaus, and G. Grübel, *J. Phys.: Conf. Ser.* **2380**, 012134 (2022).
- [47] M. Riepp, Ph.D. thesis, Universität Hamburg, 2021.
- [48] G. Winkler, A. Kobs, A. Chuvilin, D. Lott, A. Schreyer, and H. P. Oepen, *J. Appl. Phys.* **117**, 105306 (2015).
- [49] B. Koopmans, G. Malinowski, F. Dalla Longa, D. Steiauf, M. Fähnle, T. Roth, M. Cinchetti, and M. Aeschlimann, *Nat. Mater.* **9**, 259 (2010).
- [50] K. C. Kuiper, T. Roth, A. J. Schellekens, O. Schmitt, B. Koopmans, M. Cinchetti, and M. Aeschlimann, *Appl. Phys. Lett.* **105**, 202402 (2014).
- [51] *CRC Handbook of Chemistry and Physics*, 95th ed., edited by W. M. Haynes (CRC Press, Boca Raton, FL, 2014).
- [52] H. Ftouni, C. Blanc, D. Tainoff, A. D. Fefferman, M. Defoort, K. J. Lulla, J. Richard, E. Collin, and O. Bourgeois, *Phys. Rev. B* **92**, 125439 (2015).
- [53] W. S. M. Werner, K. Glantschnig, and C. Ambrosch-Draxl, *J. Phys. Chem. Ref. Data* **38**, 1013 (2009).
- [54] D. Zahn, F. Jakobs, H. Seiler, T. A. Butcher, D. Engel, J. Vorberger, U. Atxitia, Y. W. Windsor, and R. Ernstorfer, *Phys. Rev. Res.* **4**, 013104 (2022).